Progress in Propulsion Physics **11** (2019) 625-656
https://doi.org/10.1051/eucass/201911625

NUMERICAL SIMULATION OF A BACKWARD-FACING STEP COMBUSTOR USING REYNOLDS-AVERAGED NAVIER–STOKES / EXTENDED PARTIALLY STIRRED REACTOR MODEL

N. Petrova, V. Sabelnikov, and N. Bertier

ONERA — The French Aerospace Lab.
Palaiseau 91761, France

The authors adapt recently developed a large eddy simulation / extended partially stirred reactor (LES/EPaSR) model by Sabelnikov and Fureby for simulation of turbulent combustion to Reynolds-averaged Navier–Stokes (RANS) equations. The proposed RANS/EPaSR model is validated against experimental database created at ONERA for an air–methane premixed flame stabilized by a backward-facing step combustor. The RANS/EPaSR model is compared also with the following RANS-based combustion models: (*i*) quasi-laminar model with reduced chemical mechanism (QL RCM); (*ii*) premixed flamelet tabulated chemistry (PFTC) without taking into account the turbulence–chemistry interaction (TCI); and (*iii*) a PFTC with a presumed β probability density function (PDF) for a progress combustion variable.

1 INTRODUCTION

The modern energy and environmental context motivate the improvement of combustion chambers for air-breathing propulsion systems. The structure of turbulent flames in industrial combustion chambers is complex: it is governed by turbulence, two-phase injection, chemical kinetics, acoustics, and radiation. Computational fluid dynamics (CFD) is an efficient tool for combustion chamber development. Modeling the TCI is a key point in the numerical simulation of the combustion in the air-breathing engines. Turbulent combustion models, once validated by comparison with experimental data, allow, using the numerical simulations, to improve the understanding of the different physical mechanisms, in particular, flame stabilization and pollution production. The

widespread approach for calculating turbulent reactive flows is based on the RANS equations [1], despite the well-known limitations of such an approach. The RANS equations are not closed and numerous terms have to be modeled: the Reynolds stress tensor, turbulent scalar fluxes, and mean chemical source terms.

The modeling of the mean chemical source terms needs a careful consideration of the TCI and usually is considered as the main problem of moment methods in turbulent combustion. State-of-the-art in the modeling of turbulent combustion is presented, e. g., in [1, 2]. We limit ourselves mentioning the following models:

(*i*) laminar flamelet models (for premixed and nonpremixed combustion): turbulent flame brush is presented as an ensemble of thin laminar flames;

(*ii*) RANS/PDF models employing presumed PDF or transported PDF [3]; and

(*iii*) phenomenological finite rate chemistry (FRC) models such as a partially stirred reactor (RANS/PaSR) [4–6] and an eddy dissipation concept (RANS/EDC) [7–10] models.

Each of these models has certain features that limit its usability for engineering applications. Therefore, it is desirable to develop more versatile and cost-effective RANS combustion models. In this paper, with that aim, the LES/EPaSR model recently developed by Sabelnikov and Fureby [11, 12] has been adapted to the RANS simulation. It is worth to mention that PaSR model was improved as well in [5, 13] using the additional transport equations for the reactor species. The concept of the model is based on the experimental results of Batchelor and Townsend [14] showing that at high Reynolds numbers, turbulent fine structure is not uniformly distributed in space but concentrated in small isolated regions, whose volume is a small fraction of the total volume. Chomiak [15] has used these results for qualitative description of the turbulent flame, assuming that the most intensive molecular mixing, chemical reactions, and heat release take place mainly in the fine structures. Later, this model has been refined in [7–10]. The spatial no uniformity of the turbulent fine structures has been verified by a direct numerical simulation in nonreactive [16] and reactive [17, 18] flows.

The organization of the paper is as follows: the RANS/EPaSR model is presented in section 2. In section 3, the simplified assumptions introduced for that the model to be adapted to the structure of the industrial code CEDRE developed in ONERA [19]. The validation of the RANS/EPaSR model on the experimental database created at ONERA for an air–methane premixed flame stabilized by a backward-facing step combustor is presented in sections 4 and 5.

2 REYNOLDS-AVERAGED NAVIER–STOKES / EXTENDED PARTIALLY STIRRED REACTOR MODEL

2.1 Governing Equations

The EPaSR model, similar to the PaSR [4–6] and the EDC [7–10] models, is based on the assumption that at high turbulent Reynolds numbers, the chemical reactions take place essentially in the fine turbulent structures. These structures are not uniformly distributed in space and its volume is a fraction of the total gas volume. This implies that the fine-structure regions are embedded in a surrounding fluid. The most intensive molecular mixing, chemical reactions, and heat release take place mainly in the fine structures. Henceforth, the quantities inside of the fine structures and in a surrounding fluid will be denoted by * and ^{0}, respectively.

The principal difference between the EPaSR and the PasR models is that the former is formulated using differential equations for the evolution of the quantities in the fine structures and surroundings and the last is based on the algebraic equations. In other words, contrary to the PaSR model, the EPaSR model takes into account the history effects in the turbulent flow.

The derivation of the LES/EPaSR model [11,12] makes use of the similarities with the mathematical treatment of multiphase flows. The reader is referred to [11, 12] for the details. The RANS/EPaSR model is a direct modification of the LES/EPaSR model [11, 12]. The equations of the RANS/EPaSR model follow directly from the LES/EPaSR after change of characteristic turbulent time and length scales. Let us denote the composition space

$$\boldsymbol{\psi} = [\mathbf{Y}, h_s] \ .$$

Here, $\mathbf{Y} = [Y_1, \ldots, Y_{N_{\rm sp}}]$ are the mass fractions of $N_{\rm sp}$ species and h_s is the sensible enthalpy:

$$h_s = \sum_{i=1}^{N_{\rm sp}} Y_i \int_{T_0}^{T} C_{p,i}\, dT$$

where $C_{p,i}$ is the heat capacity at constant pressure of species i and T is the temperature. The evolution of $\boldsymbol{\psi}$ is governed by the local balance equations of mass fractions and total energy [1]. The Favre averages, fine structures, and surroundings quantities are related by the following expression:

$$\tilde{\boldsymbol{\psi}} = \gamma^* \boldsymbol{\psi}^* + (1 - \gamma^*)\boldsymbol{\psi}^0 \qquad (1)$$

where γ^* is the fine-structure volume fraction; and $\boldsymbol{\psi}^*$ and $\boldsymbol{\psi}^0$ are the quantities inside of the fine structures and surroundings, respectively. Also, let us denote

$\tilde{f} = \overline{\rho f}/\overline{\rho}$ to be the Favre (mass-weighted) average of f, overline designates Reynolds average.

The transport equations for $\boldsymbol{\psi}^*$ and $\boldsymbol{\psi}^0$ used in LES/EPaSR model are given in [11, 12] where it is also noted that more convenient and straightforward approach is, however, to solve the balance equations for $\boldsymbol{\psi}^*$ together with the LES balance equations for $\tilde{\boldsymbol{\psi}}$. This approach will be used for RANS/EPaSR model as well. The set of balance equations for $\boldsymbol{\psi}^*$ together with the RANS balance equation for $\tilde{\boldsymbol{\psi}}$ reads:

$$\frac{\partial \overline{\rho}}{\partial t} + \nabla \cdot (\overline{\rho}\tilde{\mathbf{u}}) = 0\,; \tag{2}$$

$$\frac{\partial \overline{\rho}\tilde{\mathbf{u}}}{\partial t} + \nabla \cdot (\overline{\rho}\tilde{\mathbf{u}}\tilde{\mathbf{u}}) = -\nabla \overline{p} + \nabla \cdot (\overline{\boldsymbol{\tau}} - \mathbf{b})\ ; \tag{3}$$

$$\frac{\partial}{\partial t}\left(\overline{\rho}\tilde{\psi}_i\right) + \nabla \cdot \left(\overline{\rho}\tilde{\mathbf{u}}\tilde{\psi}_i\right) = \nabla \cdot \left(\overline{\mathbf{k}}_i - \mathbf{b}_i\right) + \overline{\dot{\omega}}_i^*\ ,\ \ i = 1, \ldots, N_{\mathrm{sp}} + 1\,; \tag{4}$$

$$\frac{\partial}{\partial t}\left(\overline{\rho}\gamma^*\psi_i^*\right) + \nabla \cdot \left(\overline{\rho}\gamma^*\psi_i^*\tilde{\mathbf{u}}\right) = \nabla\left(\gamma^*\left(\overline{\mathbf{k}}_i - \mathbf{b}_i\right)\right) + \gamma^*\overline{\dot{\omega}}_i^* + \overline{M}_i^*\,; \tag{5}$$

$$\frac{\partial}{\partial t}\left(\overline{\rho}\gamma^*\right) + \nabla \cdot \left(\overline{\rho}\gamma^*\tilde{\mathbf{u}}\right) = \dot{m}\,; \quad \sum_{i=1}^{N_{\mathrm{sp}}} \overline{M}_i^* = \dot{m}\,; \tag{6}$$

$$\mathbf{b} = \overline{\rho\mathbf{u}\mathbf{u}} - \overline{\rho}\tilde{\mathbf{u}}\tilde{\mathbf{u}}\,,\ \ \mathbf{b}_i = \overline{\rho}\left(\widetilde{\mathbf{u}Y_i} - \tilde{\mathbf{u}}\tilde{Y}_i\right)\ ,\ \ i = 1, \ldots, N_{\mathrm{sp}}\,;$$

$$\mathbf{b}_{N_{\mathrm{sp}}+1} = \overline{\rho}\left(\widetilde{\mathbf{u}h_s} - \tilde{\mathbf{u}}\tilde{h}_s\right)$$

where p is the pressure; $\boldsymbol{\tau}$ is the viscous stress tensor; $\mathbf{b}$ if the Reynolds stress tensor; and vectors $\mathbf{k}_i$, $i = 1, \ldots, N_{\mathrm{sp}}$, and $\mathbf{k}_{N_{\mathrm{sp}}+1}$ are the molecular species mass and heat fluxes, respectively. Vectors $\mathbf{b}_i$ and $\mathbf{b}_{N_{\mathrm{sp}}+1}$ are the turbulent species mass and heat fluxes, respectively. The terms $\mathbf{b}$ and $\mathbf{b}_i$ are modeled with an eddy viscosity and diffusivity following Boussinesq approach. The exchange terms $\overline{M}_i^*$ and $\dot{m}$ in Eqs. (5) and (6) describe the exchange between the fine structures and the surroundings (through immaterial surface separating the fine structures and surroundings). The terms $\overline{M}_i^*$ and $\dot{m}$ must be modeled.

Neglecting chemical reactions in the surroundings, the mean reaction rates for the Favre-averaged species mass fractions and for the source for the Favre-averaged sensible enthalpy read:

$$\overline{\dot{\omega}}_i \approx \gamma^*\overline{\dot{\omega}}_i\left(\boldsymbol{\psi}^*\right)\ ,\ \ i = 1, \ldots, N_{\mathrm{sp}}\,;$$

$$\overline{\dot{\omega}}_{N_{\mathrm{sp}}+1} = \overline{\boldsymbol{\tau}} \cdot \nabla\tilde{\mathbf{u}} + \frac{\partial \overline{p}}{\partial t} + \tilde{\mathbf{u}} \cdot \nabla\overline{p} - \sum_{i=1}^{N_{\mathrm{sp}}} \overline{\dot{\omega}}_i\left(Y_k^*, T^*\right) h_{f,i}^0 \tag{7}$$

where $h_{f,i}^0$ is the mass enthalpy of formation of species i.

Next, let us consider briefly modeling the exchange terms $\overline{M}_i^*$ and $\dot{m}$, referring the interested reader to [11, 12]. As follows from the core physical considerations, $\overline{M}_i^*$ should contain two kinds of terms. The former term, here denoted by $\overline{\Theta}_i^*$, is due to the exchange rate of mass between the fine structures and the surroundings. If the mass exchange rate annuls, i. e., $\dot{m} = 0$ (the dynamic equilibrium state), $\overline{\Theta}_i^*$ annuls as well. The second term, here denoted by $\overline{\Omega}_i^*$, is a micromixing term. It is similar to the micromixing term in the transport equation for species PDF and in Lagrangian stochastic models of turbulent flows [3]. The term $\overline{\Omega}_i^*$ is due to molecular diffusion through the interface between the fine structures and surroundings. Indeed, even if the mass exchange rate is absent, there is exchange through the interface only due to molecular diffusion. If $\psi^* = \psi^0$, $\overline{\Omega}_i^*$, however, turns to zero as in this case, there is no molecular diffusion. Based on the above considerations, the model for the exchange terms reads:

$$\overline{M}_i^* = \overline{\Theta}_i^* + \overline{\Omega}_i^* \,, \qquad \overline{\Theta}_i^* = \frac{1}{2}\left(\dot{m} + |\dot{m}|\right)\psi_i^0 + \frac{1}{2}\left(\dot{m} - |\dot{m}|\right)\psi_i^* \,; \tag{8}$$

$$\overline{\Omega}_i^* = -\overline{\rho} C_\omega \omega \left(\psi_i^* - \psi_i^0\right) \,; \tag{9}$$

$$\dot{m} = -\frac{\overline{\rho}\left(\gamma^* - \gamma_{\text{eq}}^*\right)}{\tau^*} \tag{10}$$

where τ^* stands for the micromixing time (or the fine structure residence time); γ_{eq}^* is the equilibrium fine-structure volume fraction; $\omega = \tilde{\varepsilon}/\tilde{k}$ is the turbulent frequency with $\tilde{\varepsilon}$ being the turbulent dissipation rate and $\tilde{k}$ being the kinetic energy of the turbulence; and C_ω is the tuned constant, its value will be selected at the end of this subsection.

It can be concluded from Eq. (10) that if $\dot{m} > 0$ and $\gamma^* < \gamma_{\text{eq}}^*$, the exchange rate of mass is driven from the surroundings to the fine structures. Otherwise, if $\dot{m} < 0$ and $\gamma^* > \gamma_{\text{eq}}^*$, then the exchange rate of mass is directed from the fine structures to the surroundings. It can be emphasized that $0 < \gamma_{\text{eq}}^* < 1$ and γ^* tends to its equilibrium state with the characteristic time τ^*.

Equation (6) for the fine-structure volume fraction γ^* can be obtained summing first N_{sp} Eqs. (5) and taking into account the following identities:

$$\sum_{i=1}^{N_{\text{sp}}} Y_i^* = 1 \,; \quad \sum_{i=1}^{N_{\text{sp}}} \overline{\mathbf{k}}_i = 0 \,; \quad \sum_{i=1}^{N_{\text{sp}}} \mathbf{b}_i = 0 \,, \quad \sum_{i=1}^{N_{\text{sp}}} \overline{\omega}_i^* = 0 \,.$$

To close Eqs. (2)–(6), it is necessary also to provide closure models the equilibrium fine-structure volume fraction, γ_{eq}^* and the fine-structure residence time, τ^*. The LES/EPaSR model [11, 12] uses the following submodel for τ^*:

$$\tau^* = \sqrt{\tau_K \tau_\Delta} \,. \tag{11}$$

Here, $\tau_K = (\nu/\tilde{\varepsilon})^{1/2}$ and $\tau_\Delta = \Delta/u'$ are the Kolmogorov time scale and the subgrid velocity stretch time, respectively, where Δ and u' are the filter width and the subgrid velocity fluctuations, respectively. Similarly to Eq. (11), the micromixing time for the RANS/EPaSR can be defined as the geometric mean of the Kolmogorov time τ_K and the integral time $\tau_t = \tilde{k}/\tilde{\varepsilon} = \omega^{-1}$, that is (see also [5]),

$$\tau^* = \sqrt{\tau_K \tau_t} \tag{12}$$

The equilibrium reacting fine-structure fraction is taken from [11,12] without modification:

$$\gamma^*_{\rm eq} = \frac{\tau_{\rm ch}}{\tau_{\rm ch} + \tau^*} \tag{13}$$

where $\tau_{\rm ch}$ is the characteristic chemical time scale. For the premixed combustion, $\tau_{\rm ch}$ is taken as $\tau_{\rm ch} \approx \delta_L/S_L$ where δ_L and S_L are the laminar flame thickness and the flame speed, respectively.

In addition to the definition of the micromixing time τ^* by geometric mean, Eq. (12), another choice was tested. Namely, τ^* was taken proportional to the Kolmogorov time scale, i. e.,

$$\tau^* = C\tau_K \tag{14}$$

where C is the tuned constant. If $C = 1$, Eq. (14) is just the Kolmogorov time scale and if $C = 0.41$, one gets the fine structure residence time introduced in [7–10].

It is worth noting that the micromixing time calculated as the geometric mean, Eq. (12), is larger than calculated from Eq. (14). Therefore, $\gamma^*_{\rm eq}$, as follows from Eq. (13), is larger with use of Eq. (14).

The RANS/EPaSR model, Eqs. (2)–(6), can be simplified (similar to LES/EPaSR model [11, 12]) significantly by assuming that the unsteady, convective (left-hand side of Eq. (5)) and flux terms (first term in the right-hand side of Eq. (5)) are neglected which, in turn, implies that

$$\gamma^*\overline{\dot{\omega}}^*_i + \overline{M}^*_i = 0\,; \qquad \overline{M}^*_i = 0\,; \qquad \dot{m} = 0\,; \qquad \gamma^* = \gamma^*_{\rm eq}\,.$$

Therefore in such a limit, Eq. (5) of the RANS/EPaSR model reduces to algebraic RANS/PaSR model:

$$\overline{\dot{\omega}}_i = \gamma^*\overline{\dot{\omega}}_i(\boldsymbol{\psi}^*) = -\overline{M}^*_i = -\overline{\Omega}^*_i = \overline{\rho} C_\omega \omega(\psi^*_i - \psi^0_i)\,.$$

It should be noted that Eq. (14) coincides as well with EDC model [7–10]. Based on this observation, the constant C_ω in Eq. (9) is set to 10.5, close to the recommendation of [7–10].

2.2 Reynolds-Averaged Navier–Stokes / Extended Partially Stirred Reactor Adaption to CEDRE

The structure of CEDRE software (CFD package for diphasic reactive flows) [20] does not allow implementing directly presented in the subsection 2.1 EPaSR model for the Favre-averaged sensible enthalpy and variables for the fine structures and, therefore, requires for the original EPaSR model to be modified. In the framework of CEDRE, the mean composition space is defined as [21]

$$\tilde{\boldsymbol{\psi}} = \left[\tilde{\mathbf{Y}}, \tilde{e}_t\right] ,$$

i. e., instead of Eq. (5) for the mean sensible enthalpy, the evolution equation for Favre-averaged total energy is used. The composition space in the fine-structure regions is given by

$$\boldsymbol{\psi}^* = [\mathbf{Y}^*, h_t^*]$$

where h_t^* is the total enthalpy (which includes the mass enthalpy of formation of species). The Favre-averaged total enthalpy $\tilde{h}_t$ and the total energy $\tilde{e}_t$ are related by

$$\tilde{h}_t = \tilde{e}_t + \frac{\overline{p}}{\overline{\rho}} . \tag{15}$$

The temporal variation of the mean pressure in Eq. (7) is neglected, i. e., it is assumed that

$$\frac{\partial \overline{p}}{\partial t} \approx 0 . \tag{16}$$

The Reynolds stress tensor $\mathbf{b}$, the turbulent fluxes $\mathbf{b}_i$, $i = 1, \ldots, N_{\text{sp}}$, and $\mathbf{b}_{N_{\text{sp}}+1}$ in Eqs. (3) and (4) are closed with the Boussinesq approximation (see, e. g., [1]). For simplicity, it is assumed that the molecular diffusion coefficients D_i for species i are the same and similar assumption is done for turbulent diffusion coefficients D_{ti}, i. e.,

$$D = D_i = \frac{v}{\text{Sc}_i} ; \qquad D_t = D_{ti} = \frac{v_t}{\text{Sc}_t} . \tag{17}$$

Here, v is the kinematic viscosity; v_t is the turbulent viscosity; and Sc_i is the Schmidt number of the species i. It is assumed that the turbulent Schmidt and Prandtl numbers are equal, i. e.,

$$\text{Sc}_t = \text{Pr}_t . \tag{18}$$

Using the Boussinesq hypothesis (relations (16)–(18)), the balance equation for the Favre-averaged $\tilde{\psi}_i$ and its counterpart inside of the fine structures of species i read:

$$\frac{\partial}{\partial t}\left(\overline{p}\tilde{\psi}_i\right) + \nabla \cdot \left(\overline{p}\tilde{\mathbf{u}}\tilde{\psi}_i\right) = \nabla \cdot \left[\overline{p}(D + D_t)\nabla\tilde{\psi}_i\right] + \overline{\dot{\omega}}_i , \quad i = 1, \ldots, N_{\text{sp}} + 1 ;$$

$$\frac{\partial}{\partial t}\left(\overline{\rho}\gamma^*\psi_i^*\right) + \nabla\cdot\left(\overline{\rho}\tilde{u}\gamma^*\psi_i^*\right) = \nabla\cdot\left[\overline{\rho}(D+D_t)\nabla\gamma^*\psi_i^*\right] + \gamma^*\overline{\dot{\omega}}_i^* + \overline{M}_i^*\,,$$
$$i = 1,\ldots,N_{\rm sp}+1\,.$$

It is worth noting that the source term $\overline{\dot{\omega}^*_{N_{\rm sp}+1}}$ in the equation for h_t^* is equal to zero due to assumption (16).

3 PREMIXED FLAME STABILIZED BY A BACKWARD-FACING STEP

The proposed RANS/EPaSR model is validated against experimental database created at ONERA for an air–methane premixed flame stabilized by a backward-facing step combustor data [22,23]. The RANS/EPaSR model is compared with a few contemporary RANS combustion models such as QL RCM, PFTC no TCI, and PFTC β-PDF. It is worth nothing that the EPaSR model presented above, similar to EDC model, oversimplifies the flame–wall interaction phenomena. In particular, the special treatment of the micromixing term $\overline{\Omega}_i^*$ in Eq. (8) may be required close to the walls. Especially, it is important for water-cooled combustor (as considered in this section) to address to heat fluxes. This important problem will be considered in future.

3.1 Computational Details

3.1.1 Domain, grid, and numerical method

The geometry of the flow problem was chosen in accordance to the experimental setup of ONERA [19, 22] sketched in Fig. 1. Inlet and outlet sections of the computational domain are located at the distances 0.1 m upstream and 1 m downstream of the step, respectively. The channel height is $H = 0.1$ m downstream of the step and the height of the inflow channel is 0.065 m. The height of the step is $h = 0.035$ m. The width of the channel is $W = 0.1$ m. The origin

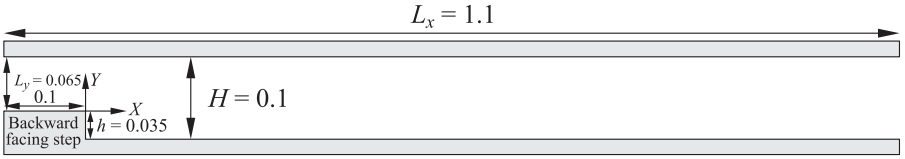

Figure 1 Sketch of the flow configuration. Dimensions are in meters

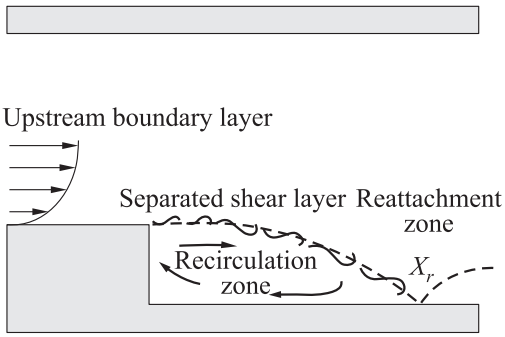

Figure 2 Principal features of a backward step flow

Table 1 Number of cells in the computational grids

Total number of cells	Number of cells	
	Before the step nose	After the step nose
$1.6 \cdot 10^4$	31×22	49×314
$2.4 \cdot 10^4$	38×25	60×384
$3.7 \cdot 10^4$	54×26	88×404
$7.7 \cdot 10^4$	74×36	123×605
$10.6 \cdot 10^4$	87×41	146×704

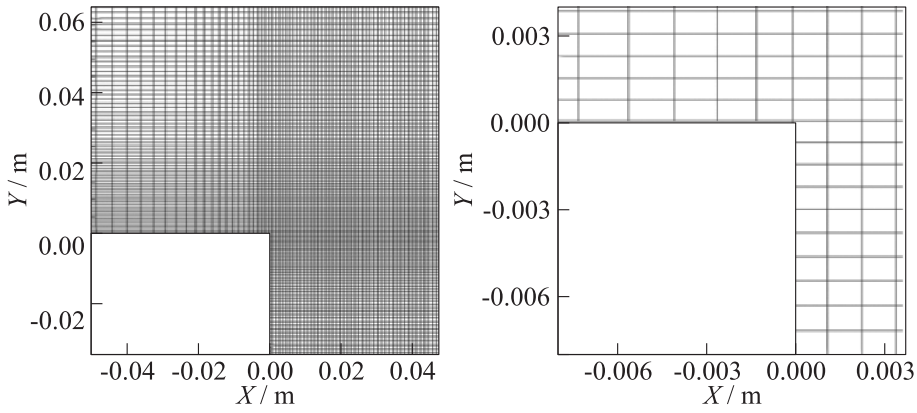

Figure 3 Two-dimensional grid for backward-facing step flow

of the reference frame $X = Y = 0$ is fixed at the nose of the step. Figure 2 represents schematically the main features of the flow. The streamwise position of the reattachment point is denoted by X_r.

The two-dimensional (2D) computations were carried out. Five computational grids composed of rectangular cells have been generated (Table 1).

These five grids have the same topology, being refined in the X and Y directions at the corner of the step and in the recirculation region. Figure 3 shows a close-up view of the step extremity of a 2D grid having $3.7 \cdot 10^4$ rectangular cells. In this study, only the results from the intermediate grid are presented as this grid has been found to result in predictions virtually identical to that of the fine grids, whereas the coarse grid shows the results that deviate slightly from the results obtained on the finer grids.

3.1.2 Boundary conditions

At the inlet, methane–air mixture is injected at the uniform temperature $\tilde{T} = 525$ K with equivalence ratio equal to 0.8. Two types of inlet conditions for the mean streamwise velocity $\tilde{u}_x$, the turbulent energy k, and the turbulent length scale l were specified:

(i) the uniform profiles $\tilde{u}_x = 58$ m/s, $\tilde{k} = 60$ m^2/s^2, and $l = 0.01$ m; and

(ii) the nonuniform profiles which simulate a fully developed turbulent channel flow upstream of the step.

These profiles were obtained by numerical simulation of the channel of height $L_y = 0.065$ m and length $L_x^{\text{channel}} = 30L_y = 1.95$ m. The grid was uniform consisting of $3 \cdot 10^2 \times 3 \cdot 10^2 = 9 \cdot 10^4$ cells. The calculation of this channel was performed with inlet velocity $\tilde{u}_x = 53$ m/s, which yielded maximum outlet velocity of approximately 58 m/s. The standard wall function method was used in the near-wall region. It is assumed that at the inlet, the fine-structure volume fraction is equal to its equilibrium value, i. e., $\gamma^* = \gamma^*_{\text{eq}}$, Eq. (13). The flux of the fine-structure volume fraction at the combustor walls was set equal to zero. The channel walls are assumed to be adiabatic. At the outlet, the pressure is set to $\overline{p} = 1$ bar. The quenching of the flame at the combustor walls was modeled letting the chemical source terms to be zero inside the first cell (0.0005 m from the wall). It should be noted that in the experiment, the combustor walls were cooled by water. The wall temperature was not measured. Assumption of adiabatic walls overestimates the gas temperature near the walls.

Figure 4 shows vertical profiles of $\tilde{u}_x$, the root-mean-square velocity fluctuations $\sqrt{2\tilde{k}/3}$ normalized by a maximal value of $\tilde{u}_x$ and the turbulent length scale l normalized by the height of the inflow channel $L_y = H - h$.

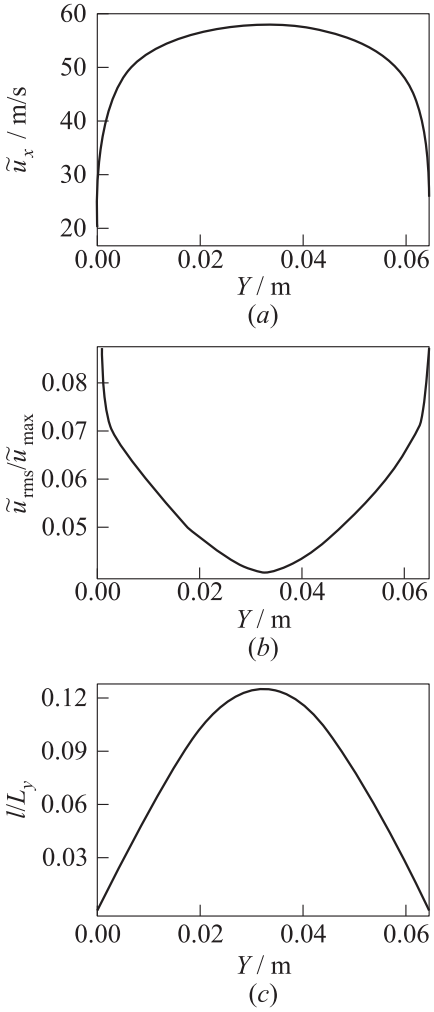

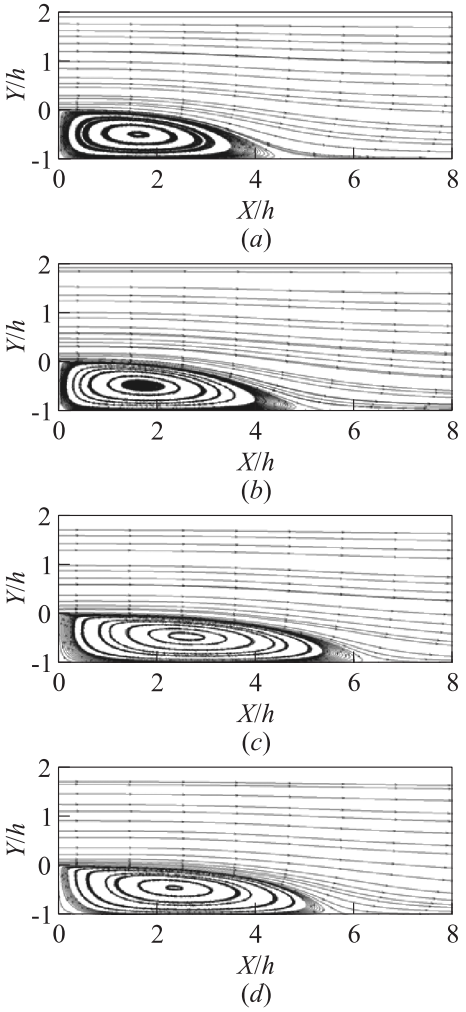

Figure 4 Calculated profiles of mean streamwise velocity $\tilde{u}_x$ (a), turbulence intensity $\sqrt{2\tilde{k}/3}/\tilde{u}_x$ (b), and turbulence length scale l/L_y (c) at the inlet section

Figure 5 Streamlines in the vicinity of the step, nonreactive case: (a) k–l (BVM) model with homogeneous inlet profiles; (b) k–l (BVM) model with nonhomogeneous inlet profiles; (c) k–ω (BVM) model with homogeneous inlet profiles; and (d) k–ω (EARSM) model with homogeneous inlet profiles

3.1.3 Turbulence models

The following models are considered for nonreactive flow case: k–l with Boussinesq viscosity model (BVM), k–ω with BVM, and k–ω with explicit algebraic Reynolds stress model (EARSM). Turbulent Prandtl and Schmidt numbers are considered to be constant: $\mathrm{Pr}_t = \mathrm{Sc}_t = 0.9$. The k–l turbulence model with BVM was employed for the reactive case. The laminar thermal conductivity and mixture viscosity are calculated with the aid of the Eucken's and the Sutherland's laws, respectively. The Schmidt numbers for all the species are assumed to be constants and equal to unity. Detailed description of the physical models can be found in CEDRE documentation [20].

4 NONREACTIVE CASE

The nonreactive backward-facing step flow calculations were performed to initialize the mean velocity, temperature, and turbulent characteristics fields, and to test the turbulence models.

The backward Euler temporal integration scheme along with the second-order monotonic upstream scheme for conservation laws scheme in space is applied. The time step is fixed to $\Delta t = 0.1$ ms.

In Fig. 5, streamline patterns are displayed, showing the size of the recirculation region behind the step for different turbulence models. It is seen that the mean reattachment of a separated flow behind the step numerical results depends on the used turbulence model.

Table 2 presents the comparison of the calculated mean reattachment lengths X_r/h obtained with different turbulence models and the experimental data [22, 23] (the error of estimation of X_r is about $\pm 0.2h$). One can conclude that the k–l turbulence model gives the best agreement with the experimental data.

Table 2 Mean reattachment length X_r in nonreactive backward-facing step flow rescaled by the step height h. The last column shows the relative error of the numerical results with respect to the experimental value

Model	X_r/h	Error
k–l (BVM)	4.83	12.3%
k–ω (BVM)	6.34	47.4%
k–ω (EARSM)	5.77	31.86%
Experiment	4.3	

Mean velocity fields have been compared with the available experimental measurements (not given here). It is found that the k–l (BVM) turbulence model yields a more accurate estimation of the velocity fields and the recirculation region length than the k–ω turbulence model (BVM or EARSM). The nonhomogeneous inlet profiles improve agreement between calculations and experimental profiles in the upper part of the chamber.

5 REACTIVE CASE

The nonuniform boundary conditions, depicted in Fig. 4, were used in the reactive case. The explicit second-order Runge–Kutta temporal integration scheme along with the first-order ODFI scheme (the Riemann invariants-based flow decentering operator scheme for hyperbolic equations) in space are applied. The time step is fixed to $\Delta t = 0.4$ μs.

5.1 Reaction Mechanism Model

Westbrook and Dryer two-step reaction mechanism of the methane combustion [24], where the oxidation of CO to CO_2 is reversible, was used for the QL RCM and EPaSR combustion models:

$$CH_4 + 1.5O_2 \rightarrow 2H_2O + CO\,;$$

$$0.5O_2 + CO \leftrightarrow CO_2\,.$$

The reverse reaction for CO_2 decomposition is used in order to reproduce proper heat release and pressure dependence of the $[CO]/[CO_2]$ equilibrium. It should be noted that the two-step reaction offers only an approximate description of methane oxidation and, in particular, overestimates the Favre-averaged temperature $\tilde{T}$ and underpredicts the ignition delay. The temperature overestimation at the equivalence ratio $\varphi = 0.8$ is relatively small (about 2%) and can be neglected. The underprediction of the ignition delay does not play in the considered simulation important role because of the use of adiabatic walls conditions. This results in the adiabatic flame temperature, $T_{\mathrm{ad}} \approx 2150$ K of the combustion products in the recirculation zone behind the step. As it can be seen from Figs. 6 and 7, T_{ad} is much larger than the temperature in the recirculation zone of the combustor with water cooled walls ($1500 < \tilde{T} < 1750$ K at $X < 0.04$ m and $1900 < \tilde{T} < 2000$ K at $X = 0.1$ m). In the simulation, the flame appears immediately downstream of the step edge in the mixing layer formed between incoming reactants flow and hot combustion products in the recirculation zone. Therefore, all turbulent combustion models tested in the present work yield more

fast axial temperature increase with respect to experimental data. The implementation of a detailed kinetic mechanism in a CFD code is still prohibitive due to the high associated computational cost. In order to partially overcome this difficulty, the flamelet tabulated chemistry (FTC) approaches were also used in two versions: (*i*) tabulated chemistry model (PFTC); and (*ii*) PFTC without TCI (no TCI).

It should be stressed that the tables are created at the base of a free laminar premixed flame without heat losses. For better predictions of the combustion, in addition to the boundary conditions taking into account the thermal fluxes at the combustor wall, new tables must be generated introducing an additional entry parameter linked with heat losses.

The FTC approaches allow performing a sufficiently accurate description of the main thermochemical phenomena with a relatively low computational cost of methane combustion modeling. The precalculated tables describe approximately the detailed chemistry by a reduced number of the transported mass fractions. The species Y_{CH_4}, Y_{O_2}, Y_{N_2}, Y_{CO}, Y_{CO_2}, and Y_{H_2O} are used in CEDRE. The methane–air reaction mechanism is taken from GRI-Mech 3.0 [25] (53 species, 325 reactions). The quasi-laminar table is done with two entry parameters: mixture fraction $\tilde{Z}$ and progress variable $\tilde{C}$. In order to generate laminar premixed FTC table, one-dimensional laminar unstretched premixed flames are first solved in physical space, for different values $\tilde{C}$, using CANTERA solver [26]:

$$\tilde{C} = \frac{\tilde{Y}_{CO} + \tilde{Y}_{CO_2}}{Y_{CO}^{eq} + Y_{CO_2}^{eq}}\,.$$

The quasi-laminar table has 200 points in $\tilde{C}$. The turbulent table has the same size as quasi-laminar but in addition, it possess 25 points in the variance progress variable space $\widetilde{C''^2}$ uniformly distributed between 0 and $\tilde{C}(1-\tilde{C})$. Afterwards, β-PDF integration is performed.

Closing this section, it is worth noting that the EPaSR model solves the equations for $\tilde{\boldsymbol{\psi}}$ and $\boldsymbol{\psi}^*$. The additional computational cost is of about 60% of the EPaSR model compared with the QL model.

5.2 Results

5.2.1 Mean temperature field

Figures 6 and 7 present the comparison of the profiles of mean temperature $\tilde{T}$ at different locations X downstream of step calculated using the EPaSR (see Fig. 6) and QL RCM and PFTC (no TCI) models (see Fig. 7) with experimental data [22, 23]. In the case of the EPaSR model, the calculations were performed with the different definitions of the micromixing time τ^*:

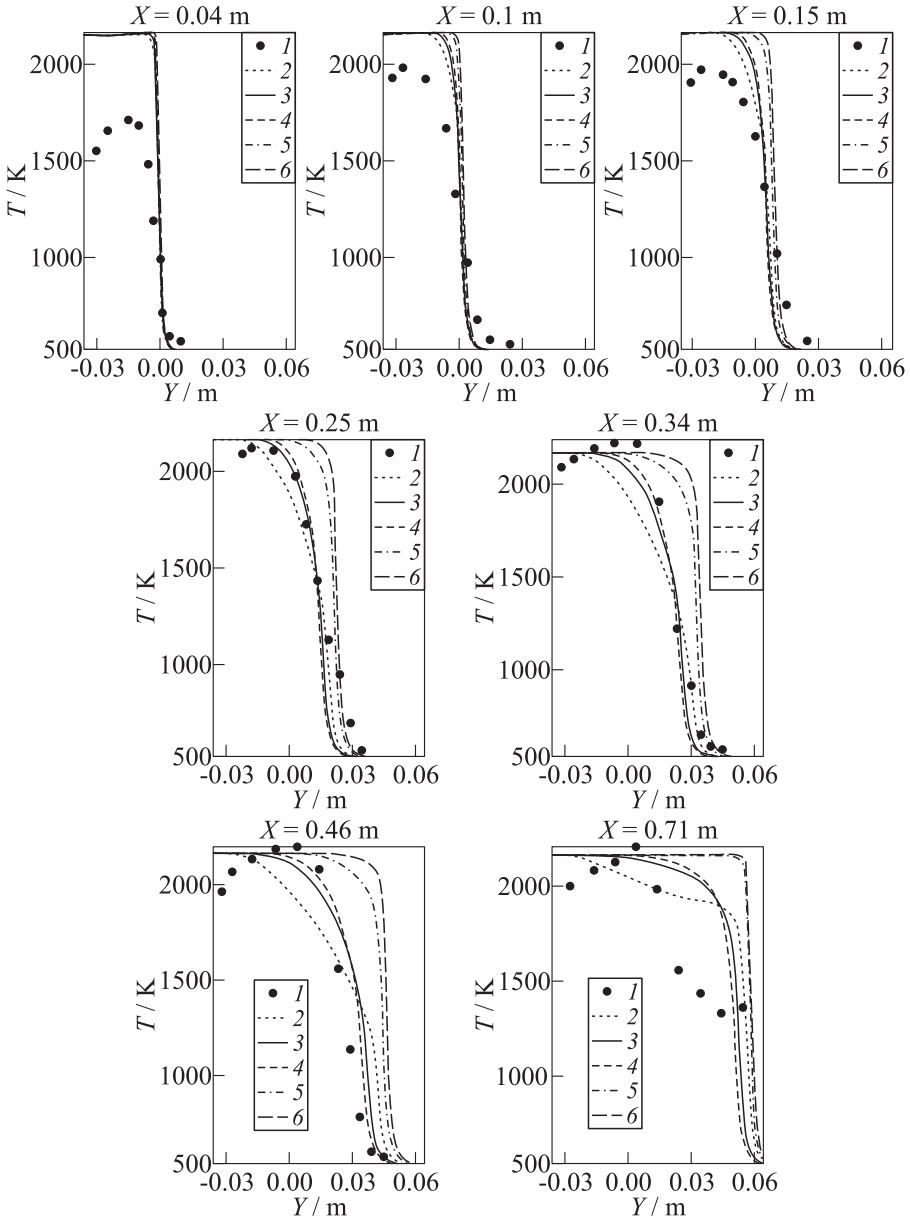

Figure 6 Profiles of Favre-averaged temperature $\tilde{T}$ in reactive backward-facing step flow; RANS/EPaSR: *1* — experiments [22, 23]; *2–4* — geometric micromixing time (*2* — $C_\omega = 5$; *3* — 10.5; and *4* — $C_\omega = 15$); *5* — Kolmogorov micromixing time, $C_\omega = 10.5$; and *6* — Magnussen micromixing time, $C_\omega = 10.5$

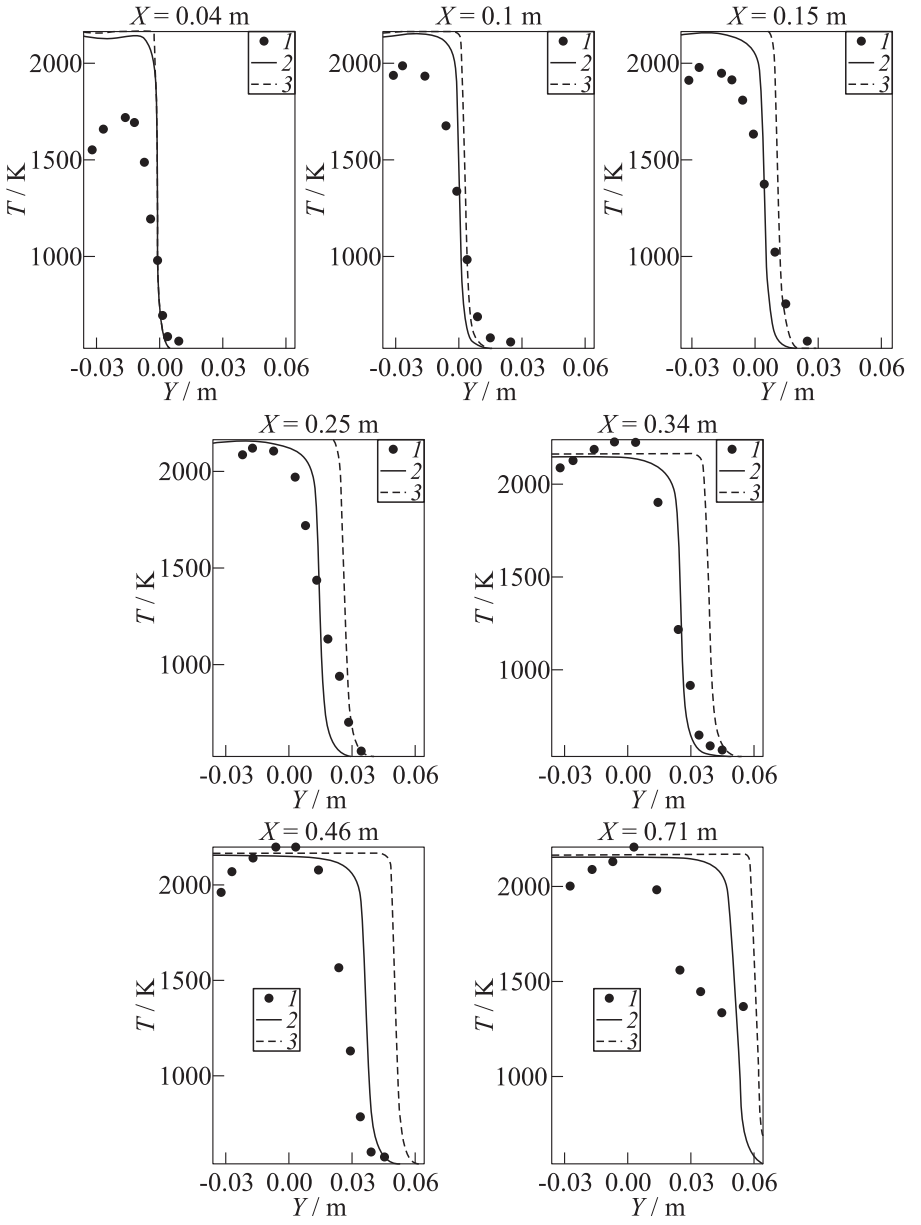

Figure 7 Profiles of Favre-averaged temperature $\tilde{T}$ in reactive backward-facing step flow; RANS/quasi-laminar approaches: *1* — experiments [22, 23]; *2* — PFTC no TCI; and *3* — QL RCM

(i) geometric mean, Eq. (12);

(ii) Kolmogorov time, $C = 1$ in Eq. (14); and

(iii) Magnussen time, $C = 0.41$ in Eq. (14).

The calculations were performed for three values of the constant C_ω in Eq. (9): 5, 10.5, and 15. It is seen that the calculated mean temperatures in the region nearby the bottom wall of the chamber ($Y < 0$) are overestimated due to using adiabatic boundary conditions. This overestimation does not depend on the combustion model. It is worth noting that for the EPasR model, the temperature overestimation can be partially explained by the underprediction of the ignition delay length.

The transverse gradient of the mean temperature $\partial\tilde{T}/\partial Y$ is very large for $X < 0.25$ m, independently on models. The calculated temperatures in the region $X < 0.25$ m exceed the experimental data. As was already discussed in subsection 5.1, it is explained by the use of adiabatic wall condition. For larger distances $0.25 \leq X < 0.71$, large temperature gradients are preserved for the QL RCM, the EPaSR with micromixing time scale defined by Kolmogorov, and Magnussen time scales, Eq. (14). The comparison of the EPaSR and the flamelets models shows that the temperature obtained with the former model is closer to the experimental data at $X = 0.46$ m.

The EPaSR model with the geometric micromixing time scale $\tau^* = \sqrt{\tau_K \tau_t}$ and $C_\omega = 10.5$ yields the best agreement with experimental data. The variation of the constant C_ω for the geometric mixing time shows the following impact on the calculated temperature. Decreasing C_ω from 10.5 to 5 results in the temperature decrease owing to the reduction of micromixing between fresh mixture and combustion products. On the contrary, increasing C_ω from 10.5 to 15 results in the temperature increase because of augmentation of the micromixing between fresh mixture and combustion products.

Figure 8 illustrates the dependence on the definition of the micromixing time τ^* on the profiles of the volume fraction of the fine structures γ^* and its equilibrium value γ^*_{eq}. the lowest γ^* and $\gamma^*_{\rm eq}$, in correspondence with the remark given at the end of subsection 2.1, are obtained for the geometric micromixing time, Eq. (12). The Magnussen definition of the micromixing time ($C = 0.41$ in Eq. (14)) yields the values of γ^* and $\gamma^*_{\rm eq}$ approximately 1.3 times larger with respect to γ^* and $\gamma^*_{\rm eq}$ calculated with the Kolmogorov scale time ($C = 1$ in Eq. (14)). In the bottom region just downstream of the step, the values of γ^* and $\gamma^*_{\rm eq}$ calculated with three different definitions of the micromixing time are lower than 0.5. Then, γ^* and $\gamma^*_{\rm eq}$ increase downstream, at $X = 0.71$ m, nearby the bottom wall $\gamma^*_{\rm eq} = \gamma^* = 0.82$ for the geometric mean micromixing time and close to $\gamma^*_{\rm eq} = \gamma^* = 0.92$ for the Magnussen and the Kolmogorov micromixing times. In the middle of the channel, γ^* is slightly larger than its equilibrium

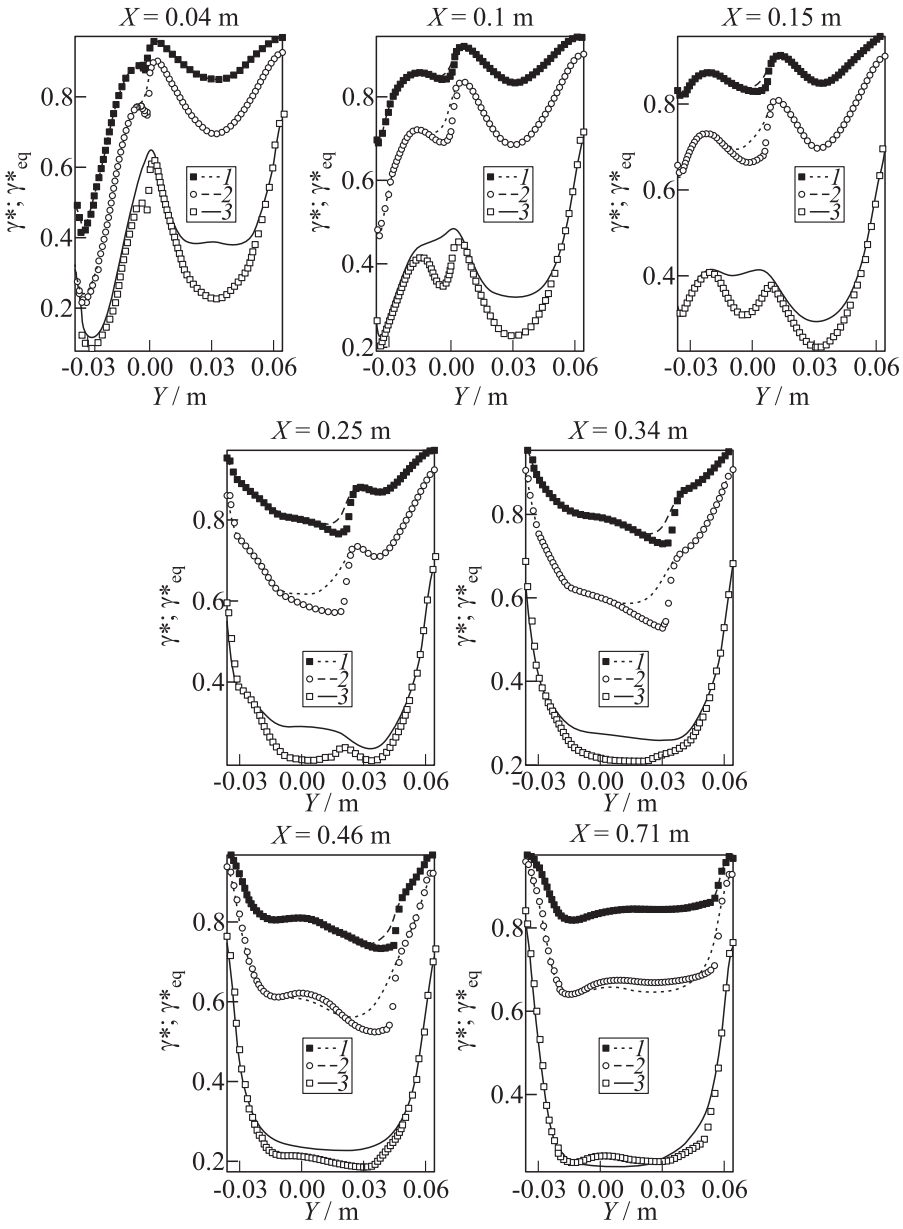

Figure 8 Profiles of volume fraction γ^* of the fine structure (curves) and its equilibrium state γ^*_{eq} in reactive backward-facing step flow (signs); RANS/EPaSR; C_ω = 10.5: *1* — Kolmogorov micromixing time; *2* — Magnussen mixromixing time; and *3* — geometric micromixing time

value $\gamma^*_{\rm eq}$ for the geometric mean micromixing time $\sqrt{\tau_K \tau_t}$. The better correspondence of the numerical predictions with experimental data obtained using the geometric mean micromixing time $\sqrt{\tau_K \tau_t}$, Eq. (12), can be explained by the lower values of γ^* with respect to the definition by Eq. (14) within the mixing layer where the chemical reactions mainly take place. It permits to smooth the temperature profile, i. e., to decrease the transverse temperature gradient $\partial\tilde{T}/\partial Y$. This effect is illustrated in Fig. 9.

Figure 9 compares the profiles of the mean temperature with the temperature in the fine structures. It is seen that the profiles of T^* are much steeper with respect to $\tilde{T}$, because $T^* > \tilde{T}$ in accordance with the relation (see Eq. (1)):

$$\tilde{T} = \gamma^* T^* + (1 - \gamma^*)\, T^0 < \gamma^* T^* .$$

Outside of the mixing layer, the impact of submodel for micromixing time weakens because the mean chemical source terms are relatively small. In addition to the calculations with the EPaSR, PFTC no TCI, and QL RCM models, the calculations with the PFTC β-PDF models were performed as well. Different closure relations were applied to dissipation and source terms in the transport equation of the combustion progress variable variance $\widetilde{C''^2}$. The best results were obtained with PFTC BML (Bray–Moss–Libby) model. In this model, the BML closure for the dissipation term in which a wrinkling factor is approximated by constant 5 and the source in the transport equation of the variance of progress variable is found directly from the table. In general, the PFTC BML overestimates the values of temperature in the combustor.

The comparison of EPaSR, QL RCM, and PFTC BML models is presented in Fig. 10. This figure shows the isolines of temperature $\tilde{T} = 1500$ K. The PFTC BML and QL RCM models overestimate the flame angle in the entire domain except the region where the flame impacts the upper wall. The flame angle calculated with the EPaSR model is close to the experimental data in the interval $0 < X < 0.4$ m. It is overestimated in the interval $0.4 < X < 0.7$ m and underestimated in the interval $0.7 < X < 0.8$ m. The divergence between the EPaSR model and experimental data nearby the combustor top wall can be explained by the use of the simple flame–wall interaction model (flame quenching) and by the behavior of γ^* nearby the wall. It is seen from Fig. 8 that the difference $1 - \gamma^*$ is small (because the ratio of two time scales $\tau^*/\tau_{\rm ch}$ in Eq. (13) decreases approaching to the walls) and, as a result, the EPaSR model reduces to the QL approach. The correspondence with the experimental data can be improved by elaborating micromixing model close to the wall.

Figure 11 shows the temperature $\tilde{T}$ field in the combustion chamber obtained with the EPaSR model with the geometric mean micromixing time, Eq. (12). The thickness and position of the flame brush are in correspondence with Figs. 6

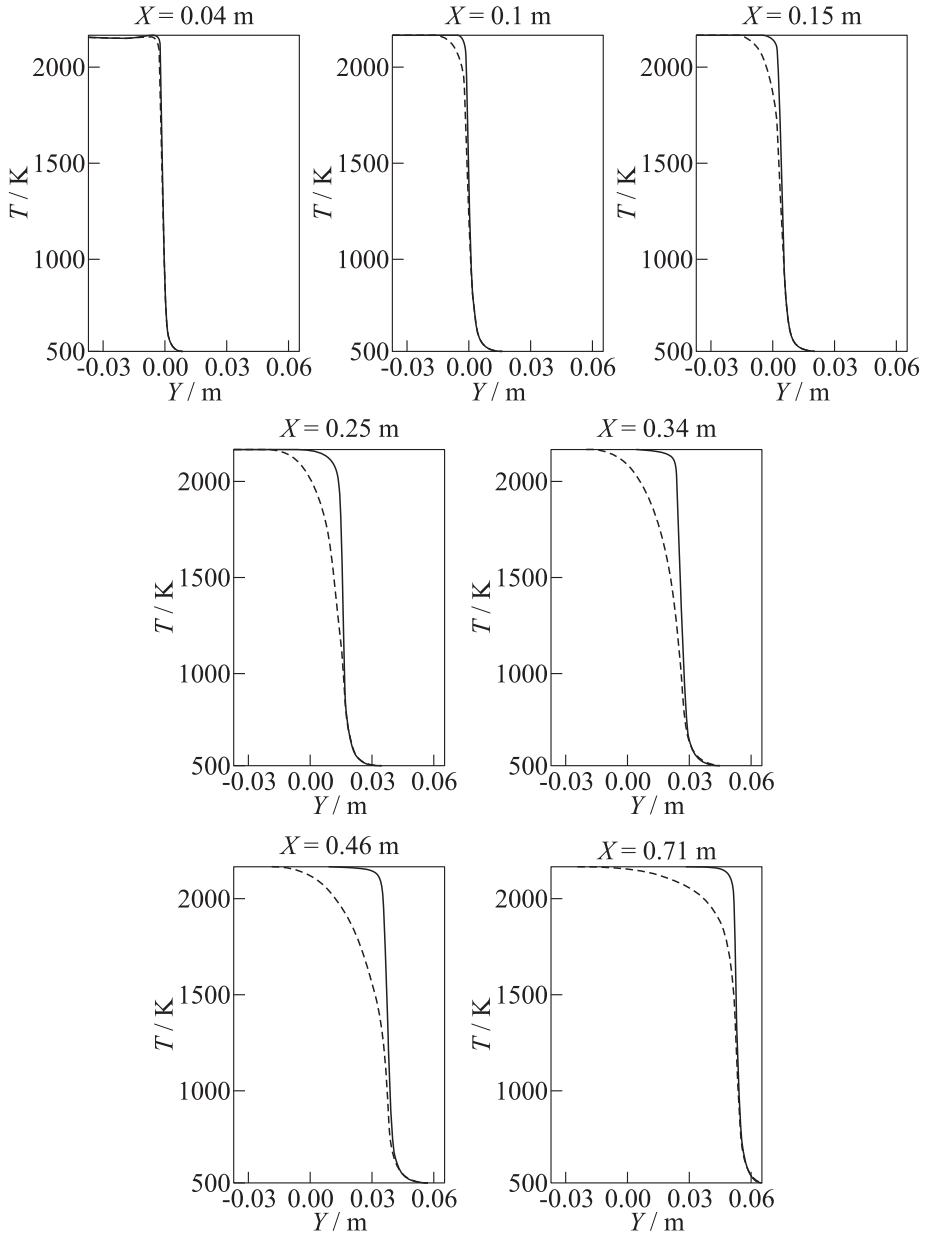

Figure 9 Comparison of the profiles of Favre-averaged temperature $\tilde{T}$ (dashed curves) and temperature in fine structures T^* (solid curves) in reactive backward-facing step flow calculated with the RANS/EPaSR model with the option "geometric micromixing time," $C_\omega = 10.5$

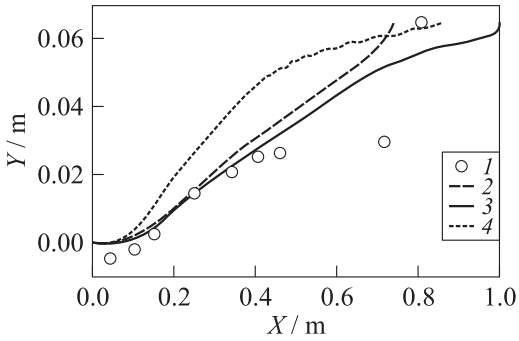

Figure 10 Isolines of temperature $\tilde{T} = 1500$ K in reactive backward-facing step flow: *1* — experiments; *2* — PFTC BML model; *3* — EPaSR, geometric micromixing with $C_\omega = 10.5$; and *4* — QL RCM

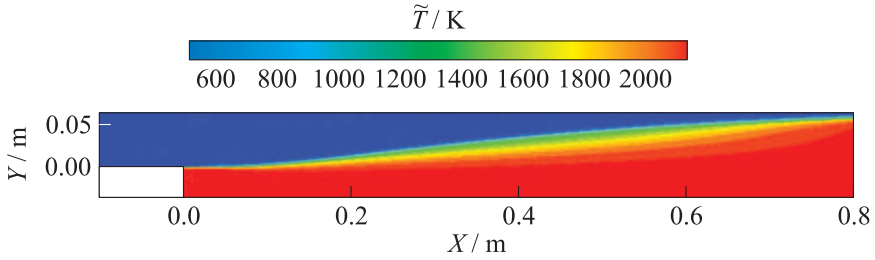

Figure 11 Field of Favre-averaged temperature $\tilde{T}$ in reactive backward-facing step flow calculated with the RANS/EPaSR model with the option "geometric micromixing time," $C_\omega = 10.5$

and 10. The possible reason of more gradual flame development with respect to the experimental data nearby the combustor top wall in the region $0.7 < X < 0.8$ m is, as was already noted, the oversimplified flame quenching model.

5.2.2 Mean velocity fields

The comparison of the calculated profiles of the mean velocity $\tilde{u}_x$ with the experimental data at different X cross sections is presented in Fig. 12 for the EPaSR model with different specifications of the micromixing time τ^*: (*i*) geometric mean, Eq. (12), for three values of C_ω: 5, 10.5, and 15 in Eq. (9) for the micromixing term; and (*ii*) Kolmogorov and Magnussen τ^*, Eq. (14), for one value of $C_\omega = 10.5$. The best correspondence with the experimental data is observed with the geometric mean micromixing time. It was found that

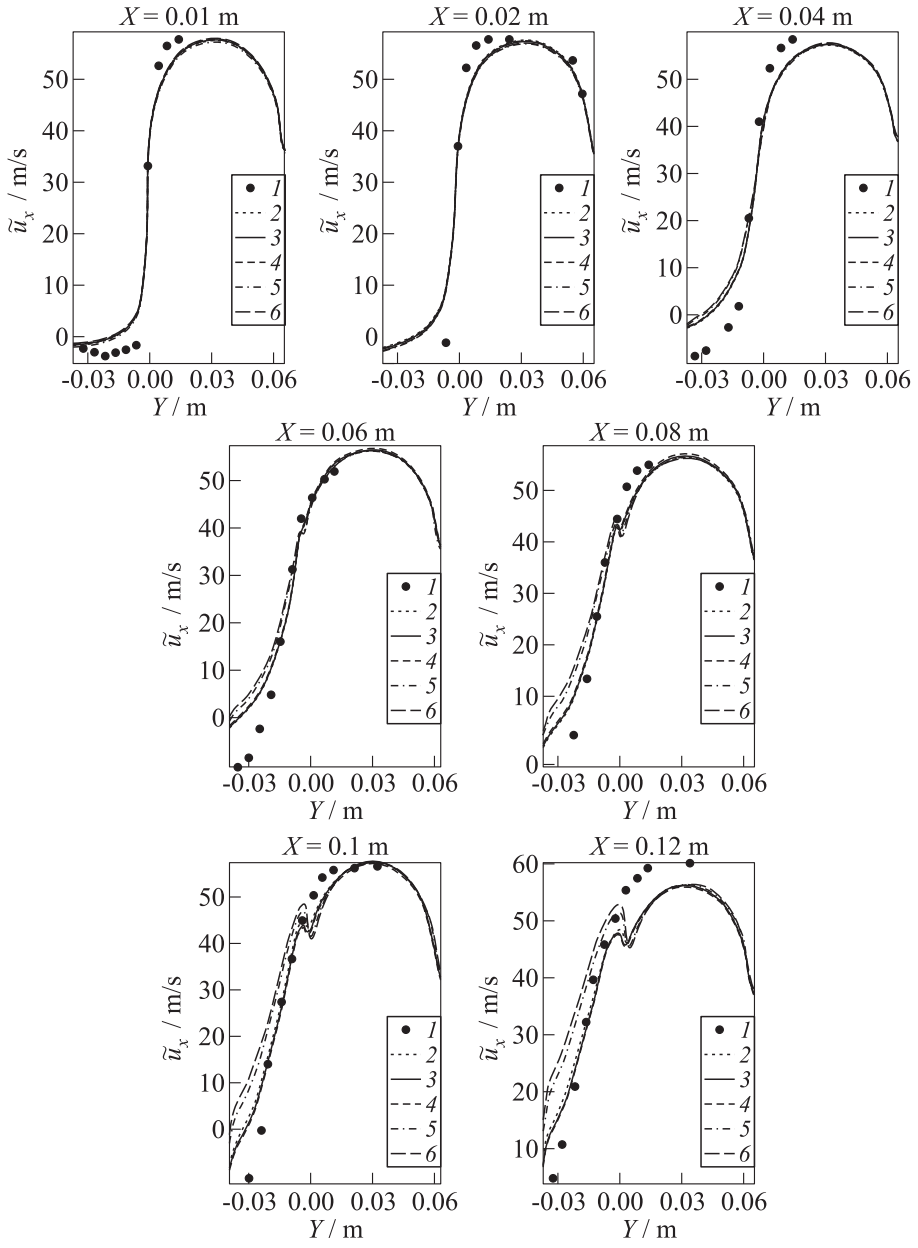

Figure 12 Profiles of Favre-averaged streamwise velocity $\tilde{u}_x$ in reactive backward-facing step flow; RANS/EPaSR: *1* — experiments; *2–4* — geometric mixromixing time (*2* — $C_\omega = 5$; *3* — 10.5; and *4* — $C_\omega = 15$); *5* — Kolmogorov micromixing time, $C_\omega = 10.5$; and *6* — Magnussen micromixing time, $C_\omega = 10.5$ (to be continued)

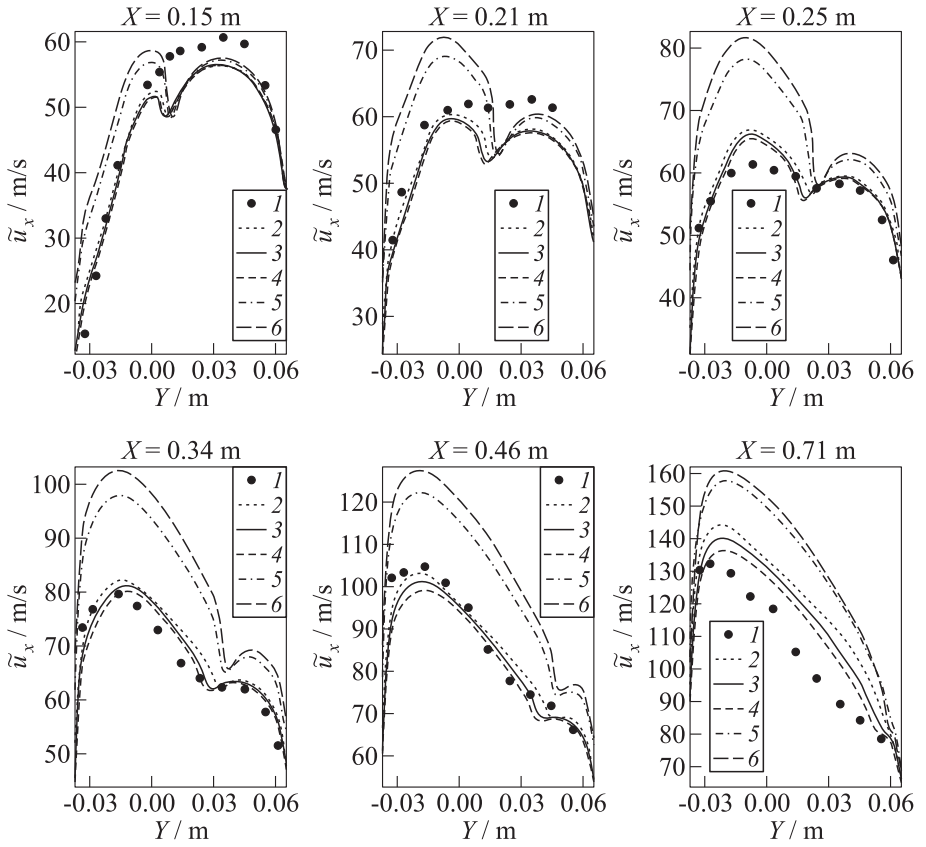

Figure 12 (continuation) Profiles of Favre-averaged streamwise velocity $\tilde{u}_x$ in reactive backward-facing step flow; RANS/EPaSR: *1* — experiments; *2–4* — geometric mixromixing time (*2* — $C_\omega = 5$; *3* — 10.5; and *4* — $C_\omega = 15$); *5* — Kolmogorov micromixing time, $C_\omega = 10.5$; and *6* — Magnussen micromixing time, $C_\omega = 10.5$

the variation of the C_ω constant has a minor importance on the mean velocity field.

Figure 13 presents the comparison of the calculated profiles of $\tilde{u}_x$ using QL RCM and PFTC no TCI with the experimental data. From Figs. 12 and 13, one may conclude that the difference between the EPaSR and PFTC no TCI models appears for $X \geq 0.25$ m. The EPaSR model with the geometric mean micromixing time yields the better results. The profiles of $\tilde{u}_x$ for the QL RCM are very similar to the EPaSR model with Kolmogorov and Magnussen micromixing times τ^*. All these models overestimate the Favre-averaged streamwise velocity.

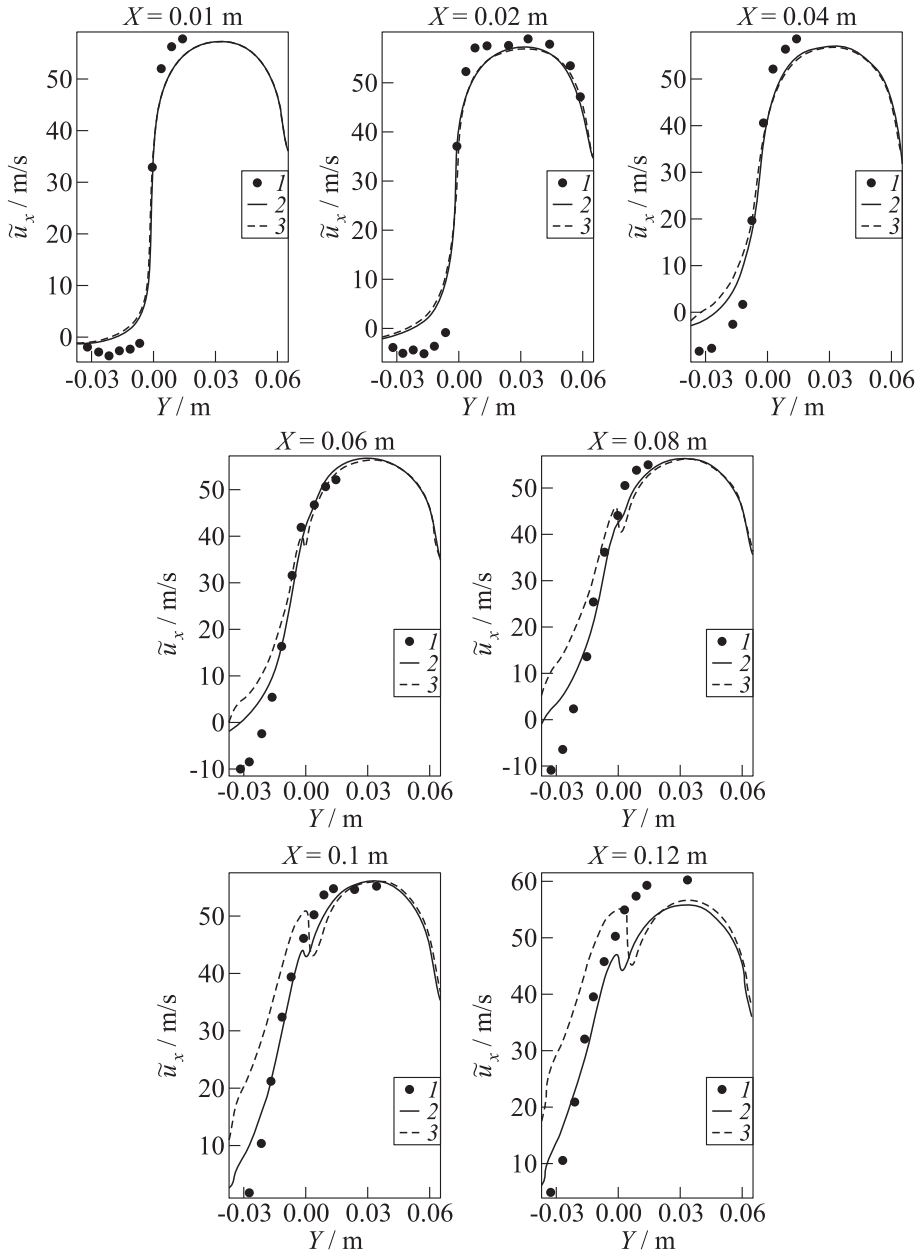

Figure 13 Profiles of Favre-averaged streamwise velocity $\tilde{u}_x$ in reactive backward-facing step flow; RANS/quasi-laminar approaches: *1* — experiments; *2* — PFTC no TCI; and *3* — QL RCM (to be continued)

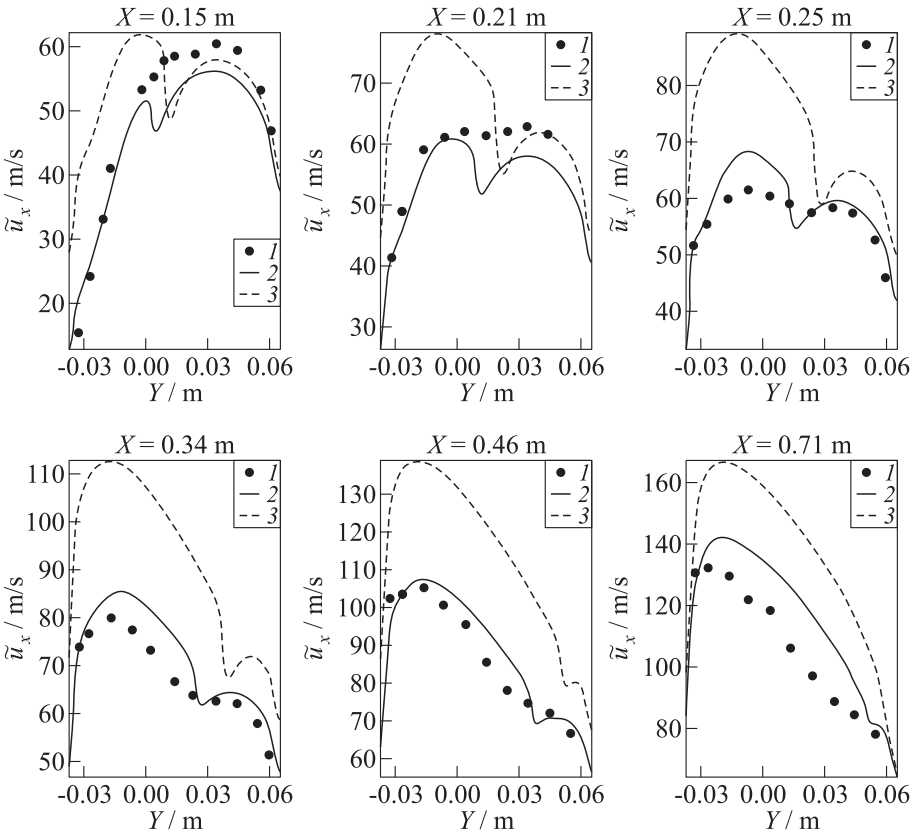

Figure 13 (continuation) Profiles of Favre-averaged streamwise velocity $\tilde{u}_x$ in reactive backward-facing step flow; RANS/quasi-laminar approaches: *1* — experiments; *2* — PFTC no TCI; and *3* — QL RCM

The comparison of the calculated profiles of the transverse mean velocity $\tilde{u}_y$, with the experimental data at different X cross sections is presented in Figs. 14 and 15.

One may observe essential difference between calculated and experimental profiles close to the step: the calculated velocity is negative at $Y > 0$ while in the experiment, it is positive. In the middle part of the combustion chamber, the calculated velocity $\tilde{u}_y$ with the geometric mean micromixing time τ^* has a satisfactory agreement with the experimental data. The peaks with minimal values of the transverse velocity are shifted to the top wall. For $X \geq 0.25$ m, the absolute values of $\tilde{u}_y$ are overestimated. The model with the Kolmogorov micromixing time better approximates the experimental results than the model

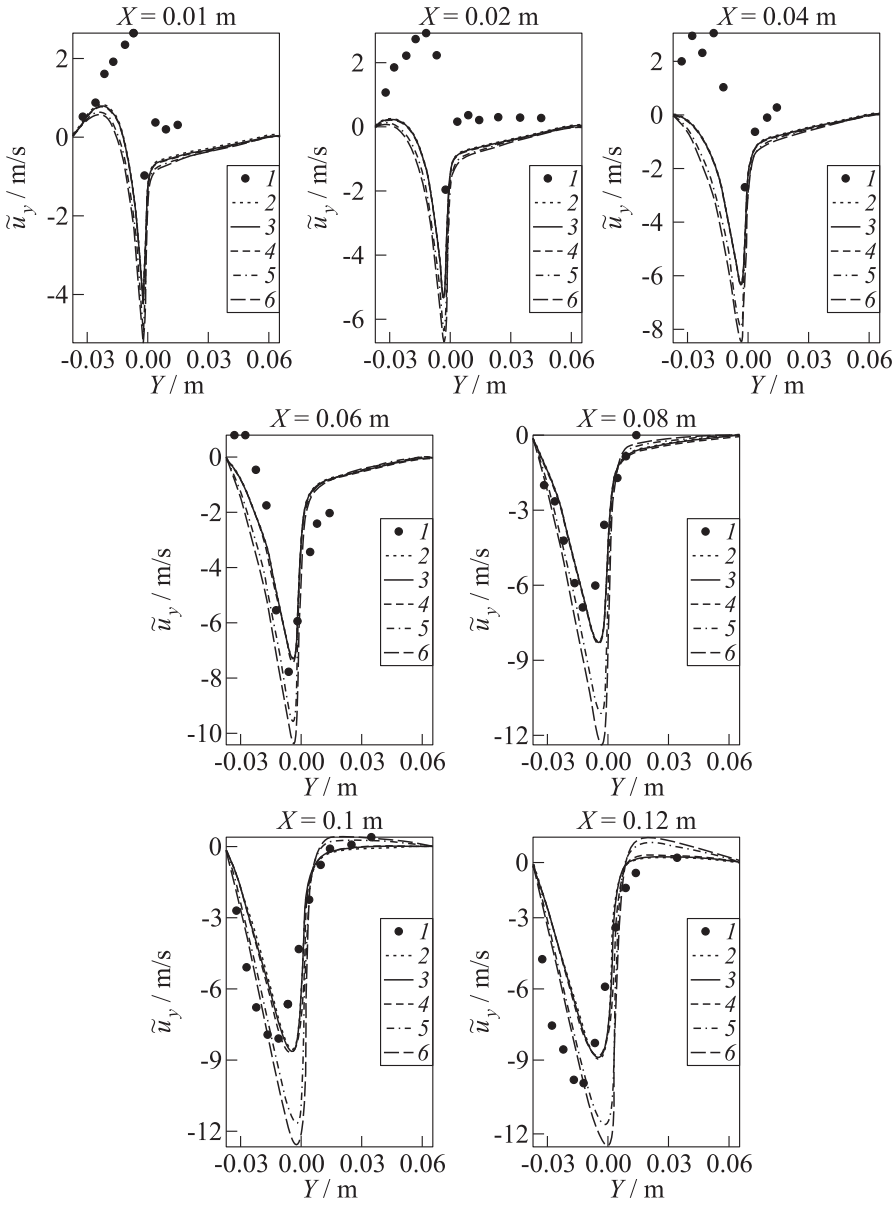

Figure 14 Profiles of Favre-averaged transverse velocity $\tilde{u}_y$ in reactive backward-facing step flow with homogeneous inlet profiles; RANS/EPaSR: *1* — experiments; *2* –*4* — geometric mixromixing time (*2* — $C_\omega = 5$; *3* — 10.5; and *4* — $C_\omega = 15$); *5* — Kolmogorov micromixing time, $C_\omega = 10.5$; and *6* — Magnussen micromixing time, $C_\omega = 10.5$ (to be continued)

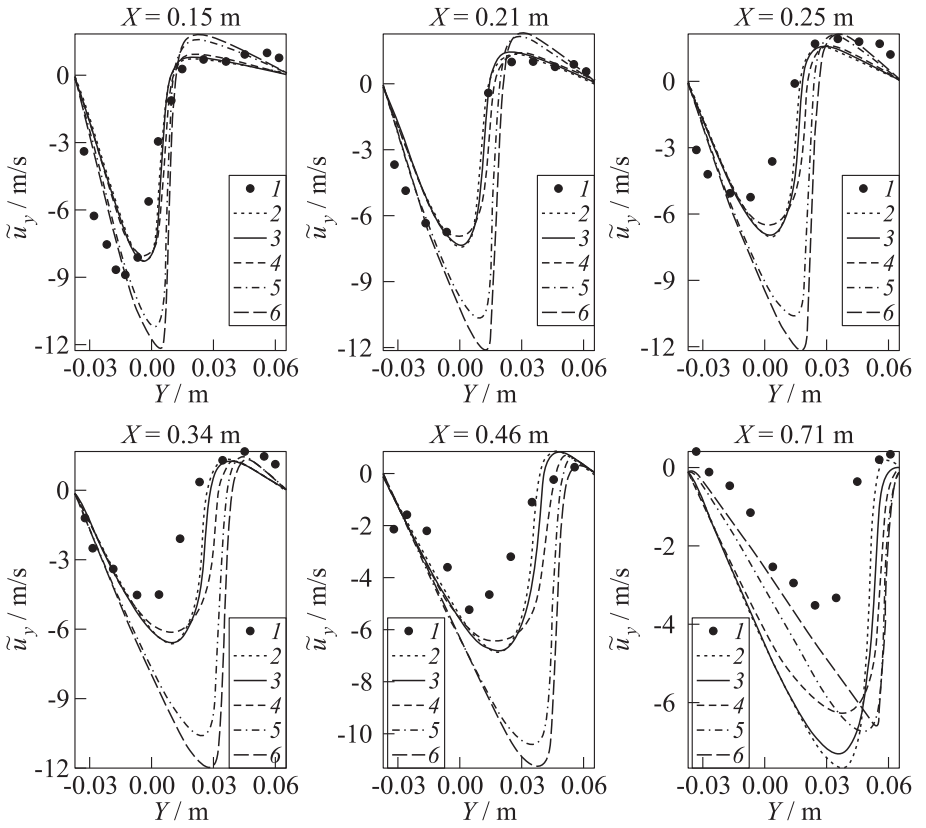

Figure 14 (continuation) Profiles of Favre-averaged transverse velocity $\tilde{u}_y$ in reactive backward-facing step flow with homogeneous inlet profiles; RANS/EPaSR: *1* — experiments; *2* –*4* — geometric mixromixing time (*2* — $C_\omega = 5$; *3* — 10.5; and *4* — $C_\omega = 15$); *5* — Kolmogorov micromixing time, $C_\omega = 10.5$; and *6* — Magnussen micromixing time, $C_\omega = 10.5$

with Magnussen micromixing time. The variation of C_ω has a minor importance on the mean transverse velocity.

It should be noted that in the experiments, the ration between the mean reattachment length X_r and the size of the step h, noted as X_r/h, is located within 2.85 and 3.42. It follows from Figs. 12–15 that X_r/h is shorter than the experimental results. In particular, for all considered models, $X_r/h < 2.7$. In the case of the EPaSR model, the relative error of the numerical results with the experimental value is about 8%–23% that is the smallest value among all the considered models. In addition, on the considered grid, none of the models captures the secondary recirculation region. This fact can explain the difference

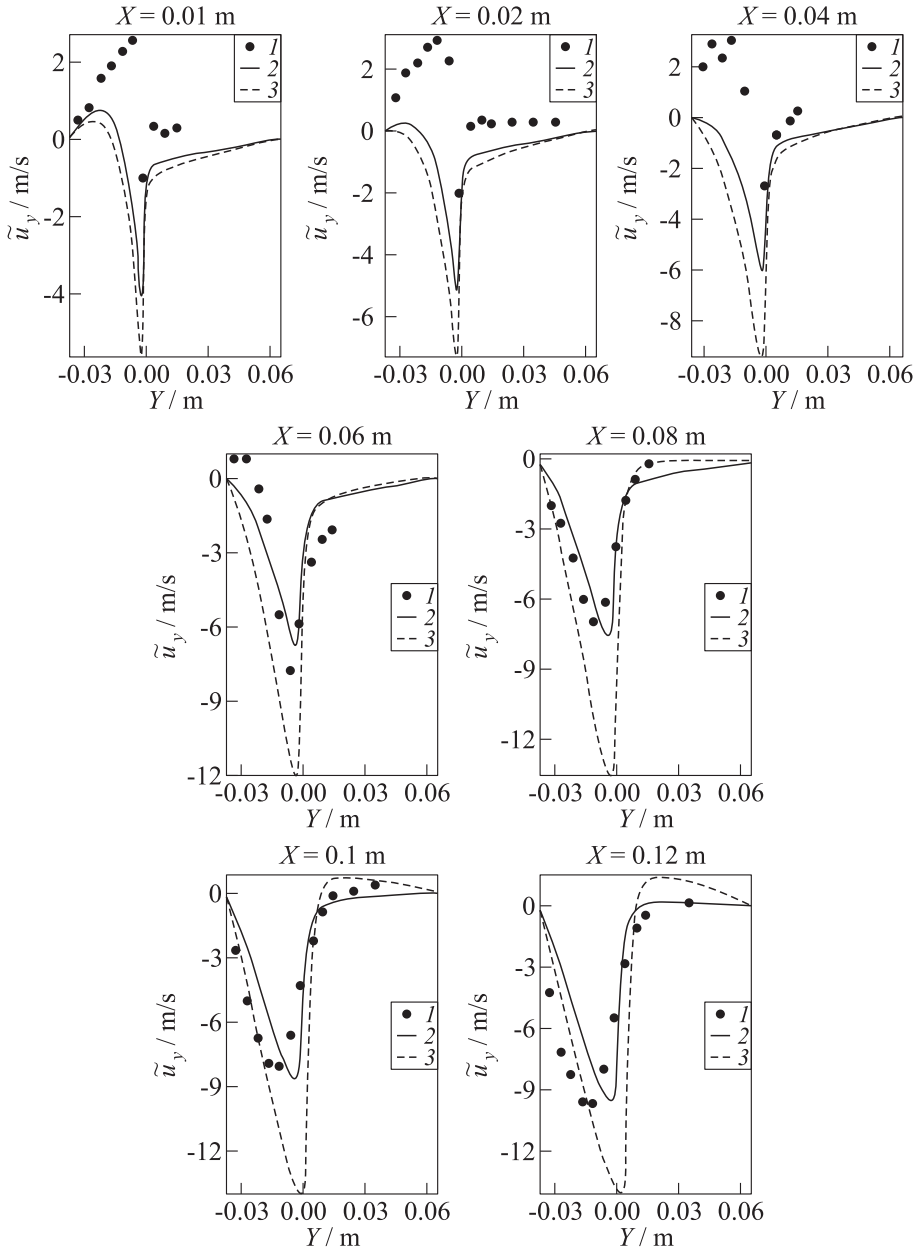

Figure 15 Profiles of Favre-averaged transverse velocity $\tilde{u}_y$ in reactive backward-facing step flow with homogeneous inlet profiles; RANS/quasi-laminar approaches: *1* — experiments; *2* — PFTC no TCI; and *3* — QL RCM (to be continued)

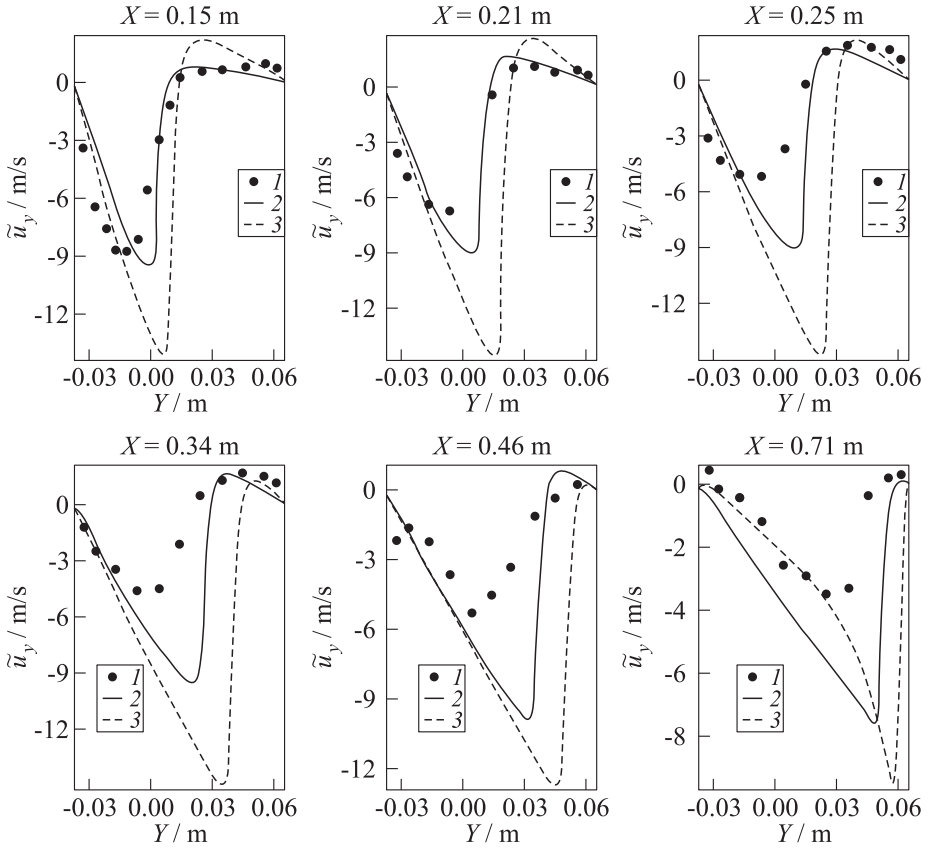

Figure 15 (continuation) Profiles of Favre-averaged transverse velocity $\tilde{u}_y$ in reactive backward-facing step flow with homogeneous inlet profiles; RANS/quasi-laminar approaches: *1* — experiments; *2* — PFTC no TCI; and *3* — QL RCM

between the numerical and experimental transverse mean velocity $\tilde{u}_y$ near the step.

6 CONCLUDING REMARKS

The present study describes and evaluates a new RANS finite rate chemistry combustion model — the RANS/EPaSR model. This model is the adaptation of the LES/EPaSR model, recently developed in [11,12]. The proposed RANS/EPaSR model is validated against experimental database created at ONERA for an air–

methane premixed flame stabilized by a backward-facing step combustor. The RANS/EPaSR model is compared also with the following RANS-based combustion models:

(*i*) QL RCM;

(*ii*) PFTC without taking into account TCI; and

(*iii*) a PFTC with a presumed (β-function) PDF for progress combustion variable.

For this combustor, the overall best performing model is the RANS/EPaSR model.

ACKNOWLEDGMENTS

Financial support for this work was provided by the Office National d'Etudes et de Recherches Aerospatiales. We acknowledge the two anonymous reviewers for their useful comments.

REFERENCES

1. Poinsot, T., and D. Veynante. 2001. *Theoretical and numerical combustion.* Philadelphia, PA: R. T. Edwards, Inc. 473 p.
2. Peters, N. 2000. *Turbulent combustion.* Cambridge University Press. 324 p.
3. Pope, S. 1985. PDF methods for turbulent reacting flows. *Prog. Energ. Combust. Sci.* 27:119–192.
4. Vulis, L. A. 1961. *Thermal rezhime of combustion.* New York, NY: McGraw-Hill. Ch. 3. (Translation from the Russian edition: 1954. *Teplovoy rezhim goreniya.* Moscow–Leningrad: Gosenergoizdat. 288 p.)
5. Chomiak, J., and A. Karlsson. 1996. Flame liftoff in diesel sprays. *26th Symposium (International) on Combustion.* Pittsburg, PA: The Combustion Institute. 2557–2504.
6. Golovitchev, V., N. Nordin, R. Jarnicki, and J. Chomiak. 2000. 3-D Diesel spray similutions using a new detailed chemistry turbulent combustion model. SAE Technical Paper No. 2000-01-1891. doi: 10.4271/2000-01-1891.
7. Magnussen, B. F., and B. H. Hjertager. 1976. On mathematical models of turbulent combustion with special emphasis on soot formation and combustion. *Symposium (International) on Combustion.* 16(1):719–729.

8. Magnussen, B. 1981. On the structure of turbulence and a generalized eddy dissipation concept for chemical reaction in turbulent flow. *19th Aerospace Sciences Meeting*. St. Louis, MO. doi: 10.2514/6.1981-42.
9. Ertesvag, I. S., and B. F. Magnussen. 2000. The eddy dissipation turbulence energy cascade model. *Combust. Sci. Techol.* 159:213.
10. Magnussen, B. F. 2005. The eddy dissipation concept: A bridge between science and technology. *ECCOMAS Thematic Conference on Computational Combustion*. 21–24.
11. Sabelnikov, V., and C. Fureby. 2013. LES combustion modeling for high Re flames using a multi-phase analogy. *Combust. Flame* 160:83–96.
12. Sabelnikov, V., and C. Fureby. 2013. Extended LES-PaSR model for simulation of turbulent combustion. *Progress in propulsion physics*. Eds. L. DeLuca, C. Bonnal, O. Haidn, and S. Frolov. EUCASS advances in aerospace sciences ser, TORUS PRESS – EDP Sciences. 4:539–568.
13. Kosters, A., V. Golovitchev, and A. Karlsson. 2012. A numerical study of the effect of EGR on flame lift-off in n-heptane sprays using a novel PaSR model implemented in OpenFOAM. *SAE Int. J. Fuels Lubr.* 5(2):604–610. doi: 10.4271/2012-01-0153.
14. Batchelor, G. K., and A. A. Townsend. 1949. The nature of turbulent motion at large wave-numbers. *Proc. Roy. Soc. Lond. A Mat.* 199:238.
15. Chomiak, J. 1970. A possible propagation mechanism of turbulent flames at high Reynolds numbers. *Combust. Flame* 15:319.
16. Woodward, P. R., D. H. Porter, I. Sytine, S. E. Anderson, A. A. Mirin, B. C. Curtis, R. H. Cohen, W. P. Dannevik, A. M. Dimits, D. E. Eliason, K.-H. Winkler, and S. W. Hodson. Very high resolution simulations of compressible turbulent flows. *Computational fluid dynamics. 4th UNAM Supercomputing Conference Proceedings*. Eds. E. Ramos, G. Cisneros, A. Fernandez-Flores, and A. Santillan-Gonzalez. World Scientific. 13 p.
17. Tanahashi, M., M. Fujimura, and T. Miyauchi. 2000. Coherent fine scale eddies in turbulent premixed flames. *Proc. Combust. Inst.* 28:5729.
18. Tanahashi, M., M. Sato, M. Shimura, and T. Miyauchi. 2008. DNS and combined laser diagnostics of turbulent combustion. *J. Therm. Sci. Tech. Jpn.* 3:391.
19. Refloch, A., B. Courbet, A. Murrone, *et al.* CEDRE software. 10 p. Available at: http://www.aerospacelab-journal.org/sites/www.aerospacelab-journal.org/files/AL2-11.pdf (accessed August 11, 2017).
20. Chevalier, P., B. Courbet, D. Dutoya, P. Klotz, E. Ruiz, J. Troyes, and P. Villedieu. 2005. CEDRE: Development and validation of a multiphysics computational software. *1st European Conference for Aerospace Sciences Proceedings*.
21. Petrova, N. 2015. Turbulence–chemistry interaction models for numerical simulation of aeronautical propulsion systems. Ecole Polytechnique. PhD Thesis.
22. Moreau, P., J. Labbe, F. Dupoirieux, and R. Borghi. 1985. Experimental and numerical study of a turbulent recirculation zone with combustion. *5th Symposium on Turbulent Shear Flows*. 1.

23. Magre, P., P. Moreau, G. Collin, R. Borghi, and M. Péalat. 1988. Further studies by CARS of premixed turbulent combustion in a high velocity flow. *Combust. Flame* 71(2):147–168.

24. Westbrook, C. K., and F. L. Dryer. 1981. Simplified reaction mechanisms for the oxidation of hydrocarbon fuels in flames. *Combust. Sci. Technol.* 27(1-2):31–43.

25. Smith, G. P., D. M. Golden, M. Frenklach, N. W. Moriarty, B. Eiteneer, M. Goldenberg, C. T. Bowman, R. K. Hanson, S. Song, W. C. Gardiner, Jr., V. V. Lissianski, and Z. Qin. GRi-Mech. Available at: http://www.me.berkeley.edu/gri_mech/ (accessed August 11, 2017).

26. Goodwin, D. G., H. K. Moffat, and R. L. Speth. 2014. Cantera: An object-oriented software toolkit for chemical kinetics, thermodynamics, and transport processes. Ver. 2.2.1. Available at: https://zenodo.org/record/45206 (accessed March 21, 2018).